Numerical Simulations of the Atmospheric Response to a Sea Surface Temperature Anomaly over the Equatorial Eastern Pacific Ocean

CARLOS R. MECHOSO, AKIO KITOH*, SHRINIVAS MOORTHI AND AKIO ARAKAWA

Department of Atmospheric Sciences, University of California, Los Angeles, CA 90024

(Manuscript received 5 January 1987, in final form 22 April 1987)

ABSTRACT

The atmospheric response to a sea surface temperature anomaly over the equatorial eastern Pacific Ocean (SSTA) is investigated using the UCLA General Circulation Model. The SSTA used is an idealization of that compiled by Rasmusson and Carpenter for the mature phase of El Niño. Two simulations over seasons, one without and the other with the SSTA, are performed and their results are compared for the Northern Hemisphere winter season.

In the tropics, the SSTA enhances precipitation over the central and eastern equatorial Pacific, while it decreases precipitation over the adjacent regions. The anomalous precipitation is predominantly balanced by the anomalous moisture flux convergence, which has comparable magnitude in the planetary boundary layer (PBL), and in the free atmosphere with quite different geographical distribution. This suggests that the anomalous precipitation, and hence the anomalous tropical cumulus heating, cannot be related exclusively to either flow anomalies in the PBL or in the free atmosphere.

In the midlatitudes, it is found that the SSTA results in a more zonal flow over the Pacific with an intensification of the upper-tropospheric westerlies. Associated with this intensification, synoptic-scale transient baroclinic waves become more active. This is consistent with interannual differences in observed spectral distributions of transients for five winters, two of which were El Niño winters. Geographically, the increase in baroclinic wave activity occurs in a zonal belt extending from the northeastern Pacific to the northern Atlantic.

1. Introduction

There is no doubt that surface conditions such as sea surface temperature (SST), albedo, ground wetness, ice and snow cover over land, and sea ice, strongly influence the long-term behavior of the atmosphere. Their geographical distribution is the result of complicated interactions between the atmosphere, the oceans, the land, the cryosphere and the biosphere. But even when surface conditions are known as functions of space and time, their effect on the atmosphere is not well understood.

El Niño–Southern Oscillation (ENSO) is essentially an air–sea interaction phenomenon. As a first step, however, ENSO can be studied as a problem of the influence of surface conditions on the atmosphere. Several authors have used atmospheric general circulation models (GCMs), in which SSTs are prescribed, to compare the simulated atmospheric circulation with and without SST anomalies that are similar to those observed during El Niño events. Julian and Chervin (1978) used a version of the National Center for Atmospheric Research (NCAR) GCM for experiments in the perpetual-January mode with and without a SST anomaly over the equatorial eastern Pacific Ocean. Keshavamurty (1982) used a version of the Geophysical Fluid Dynamic Laboratory (GFDL) GCM for experiments over the Northern Hemisphere summer with SST anomalies over the eastern, central and western equatorial Pacific, and compared the results with those obtained from a 15-yr simulation without SST anomalies. Blackmon et al. (1983) used a version of the NCAR Community Climate Model (CCM) for experiments in the perpetual-January mode with and without a SST anomaly representative of the mature phase of El Niño. Shukla and Wallace (1983) used a version of the NASA/GLAS GCM for experiments over the Northern Hemisphere winter with and without a SST anomaly based on the compilation by Rasmusson and Carpenter (1982). Geisler et al. (1985) also used the NCAR CCM for experiments in the perpetual-January mode on the sensitivity of the atmospheric response to the magnitude and position of SST anomalies over the equatorial Pacific. Tokioka et al. (1985a) used a version of the GCM at the Meteorological Research Institute (MRI) for experiments over the Northern Hemisphere summer with and without the SST anomaly observed during the 1982–83 El Niño event. Tokioka et al. (1985b) also used the MRI GCM for experiments in the perpetual-January mode with and without an SST anomaly based on the compilation by Rasmusson and Carpenter (1982). Palmer and Mansfield (1986a,b) used a version of the United Kingdom

* Present affiliation: Meteorological Research Institute, Tsukuba, 305 Japan.

Meteorological Office model, again in the perpetual-January mode, and discussed the impact of model climatology and the variability of the seasonal mean response. These experiments have shown that warm equatorial SST anomalies result in increased tropical precipitation, which is mostly balanced by increased moisture flux convergence. They have also shown that the anomalies generate a teleconnection pattern between the tropics and extratropics that resembles the Pacific-North American (PNA) pattern and that this teleconnection pattern depends on the geographical distribution of the anomalies as well as the model climatology.

In this paper we investigate the atmospheric response to a sea surface temperature anomaly over the equatorial eastern Pacific (SSTA) using the high-resolution 9-layer version of the UCLA GCM. The SSTA we used is an idealization of that compiled by Rasmusson and Carpenter (1982) for the mature phase of El Niño. We performed two simulations over seasons, one with prescribed (time-varying) "normal" SST (the control experiment), and the other with the SSTA superimposed (the anomaly experiment). In comparing the results, we concentrate on the Northern Hemisphere winter.

The UCLA GCM is significantly different from most of the models used for the experiments mentioned above, primarily due to its unique formulations of the planetary boundary layer (PBL) and moist convective processes. These are precisely the processes which are expected to play key roles in determining the overall response of the atmosphere to surface conditions. The atmosphere recognizes surface conditions through turbulent and radiative fluxes, the former having a direct effect only in the PBL. The coupling between the free atmosphere and the surface, therefore, is indirect, involving interactions between the free atmosphere and the PBL. Such interactions can produce positive feedbacks, especially when deep cumulus clouds are involved. It is clear, therefore, that the unique formulations of the PBL and moist-convective processes in the UCLA GCM provide sufficient motivation for this investigation. In addition, we use a relatively high horizontal resolution to better represent cyclone-scale motions which are a significant component of the mid-latitude atmospheric response to the SSTA.

We begin in section 2 by giving an outline of the UCLA GCM. Section 3 presents a description of our experiments. Section 4 provides a brief description of winter simulation in the control experiment. The tropical and global responses to the SSTA are presented in sections 5 and 6, respectively.

2. Outline of the UCLA GCM

The prognostic variables of the UCLA GCM are the horizontal velocity, the potential temperature, the water vapor mixing ratio, the ozone mixing ratio, the surface pressure, the PBL depth and the ground temperature.

Since PBL processes play key roles on the atmospheric response to the surface conditions (as mentioned earlier), we begin by briefly describing the approach followed in parameterizing the PBL. Observations show that for a wide range of important situations, the PBL may be regarded as a distinct and clearly identifiable part of the atmosphere. If we take advantage of this fact, the problem of PBL parameterization can be greatly simplified by making use of bulk assumptions in the description of the turbulence. An obvious difficulty in this approach is that a bulk description of the turbulence is not likely to be adequate when the boundary layer is not clearly defined. However, this occurs only when the turbulence is weak and the PBL is thin, and as long as the parameterization recognizes this, the details of the turbulence flux profiles in the thin layer will be of little consequence. The advantage of this approach is that processes near the PBL top that are responsible for interactions between the free atmosphere and the PBL can be explicitly formulated without extremely high vertical resolutions. These considerations led us to follow the bulk approach in developing the current UCLA GCM (Suarez et al., 1983).

When the top of the PBL is above the condensation level, it has a sublayer of stratocumulus clouds. The parameterization of cumulus convection and its interaction with the PBL is based on Arakawa and Schubert (1974). Surface fluxes of sensible heat, moisture and momentum are modeled with the bulk parameterization proposed by Deardorff (1972). The entrainment of mass at the PBL top is calculated using Randall's (1979) closures. In addition to the surface drag, the model includes the effects of vertical redistribution of momentum by cumulus clouds.

In the vertical, the GCM is based on a modified σ-coordinate system for which the lower boundary, the PBL top, and isobaric surfaces above a prescribed pressure level (100 mb) are coordinate surfaces. The vertical finite-differencing used above the PBL is that described by Arakawa and Suarez (1983). It guarantees conservations of the global mass integrals of potential temperature and total potential plus kinetic energy under frictionless adiabatic processes. The equations are horizontally discretized using a staggered latitude–longitude grid. The scheme for the horizontal advection terms in the momentum equation is based on the potential enstrophy conserving scheme presented by Arakawa and Lamb (1981), modified to give fourth-order accuracy for the advection of potential vorticity. The horizontal advection scheme used for the potential temperature is partially fourth-order and conserves the global mass integral of its square. The scheme for the horizontal advection of water vapor and ozone is based on the same formulation, although exact fourth-order accuracy is abandoned in favor of a formulation that prevents the occurrence of negative values. In all other terms, including the continuity equation, the pressure

gradient force, and the definition of absolute vorticity, the differencing is of second-order accuracy.

The GCM includes both diurnal and seasonal changes. The geographical distributions of surface albedo, ground wetness, and sea surface temperature are interpolated from prescribed monthly means based on the observed climatology.

We are using 15-layer and 9-layer versions of the GCM with low and high horizontal resolutions (5° long by 4° lat and 3° long by 2.4° lat, respectively). The 15-layer version has the top at 1 mb and six layers above 51.8 mb (with interfaces at 26.8, 13.9, 7.20, 3.73 and 1.93 mb), resulting in a stratospheric resolution of about 5 km. The 9-layer version has the top at 51.8 mb and is identical to the 15-layer version below that level, except that the mixing ratio of ozone is prescribed.

The GCM has been evaluated in terms of long-term simulations of monthly mean fields. Suarez et al. (1983) presented a July simulation with the low-resolution 9-layer version. A more extensive evaluation of that version in terms of a three-year simulation has been performed by Randall et al. (1985). The high-resolution 15-layer and 9-layer versions have also been evaluated by performing simulations over several months. The GCM has also been evaluated by performing a series of medium-range (10-day) predictions. In particular, the predictability of the stratospheric warming events during the winter of 1979 has been examined in detail (Mechoso et al., 1985). We have also studied tropospheric predictability, such as that of blocking events (Mechoso et al., 1986).

3. Description of the experiments

In this study, we use the high-resolution 9-layer version of the UCLA GCM to perform a pair of control-anomaly experiments. The control experiment consists of a 9½ month integration with prescribed (time-varying) climatological SST. The initial conditions for the control experiment are taken from those observed for 1 June 1979.

The SSTA used for the anomaly experiment is shown in Fig. 1. It is symmetric about the equator with a maximum value of 3°C at 120°W. This SSTA is an idealization of that for the mature phase of El Niño compiled by Rasmusson and Carpenter (1982). It excludes, among many other features, all cold anomalies. The maximum value of 3°C is larger than that found in Rasmusson and Carpenter (1982), which is for an ensemble of six events, but is comparable to that typically observed for strong El Niño events.

We performed two preliminary runs to evaluate the way in which the model atmosphere responds to different time evolutions of the SSTA before deciding on the "anomaly" experiment. These runs started from initial conditions corresponding to 15 August of the control experiment and were two months long. In the first run, the full SSTA was introduced from the beginning and kept constant in time. In the second run, the SSTA was introduced linearly in time over the first one-month period, and thereafter kept constant in time. We found that, although the different procedures for introducing the SSTA did not produce significant differences, the evolution of the tropical flow in the second run was slightly more gradual than in the first run. Based on these results, the second run was extended to cover an additional five months, which include the Northern Hemisphere winter season. In what follows, this 7-month run is referred to as the "anomaly" experiment.

4. Winter simulation in the control experiment

In this section selected results of the winter (December–February) simulation of geopotential and wind fields in the control experiment are compared with ob-

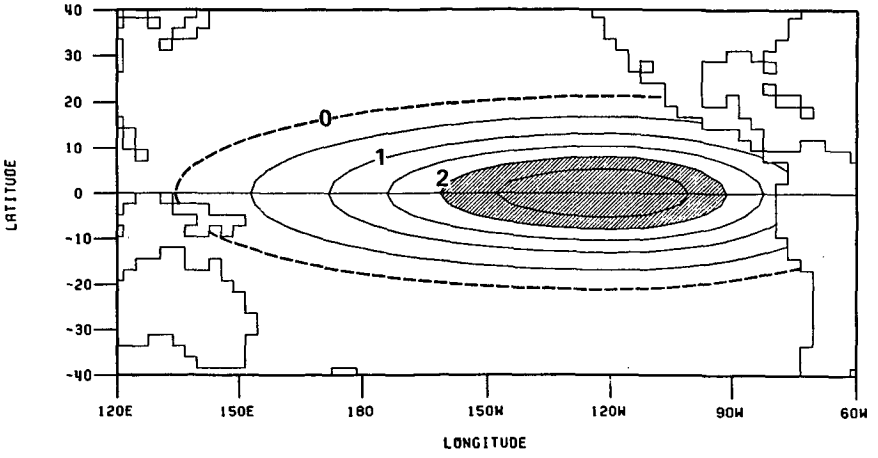

FIG. 1. Sea surface temperature anomaly SSTA (K) used in this study. Contour interval: 0.5 K. The dashed line is the boundary of the anomalous region; values greater than 2 K are shaded.

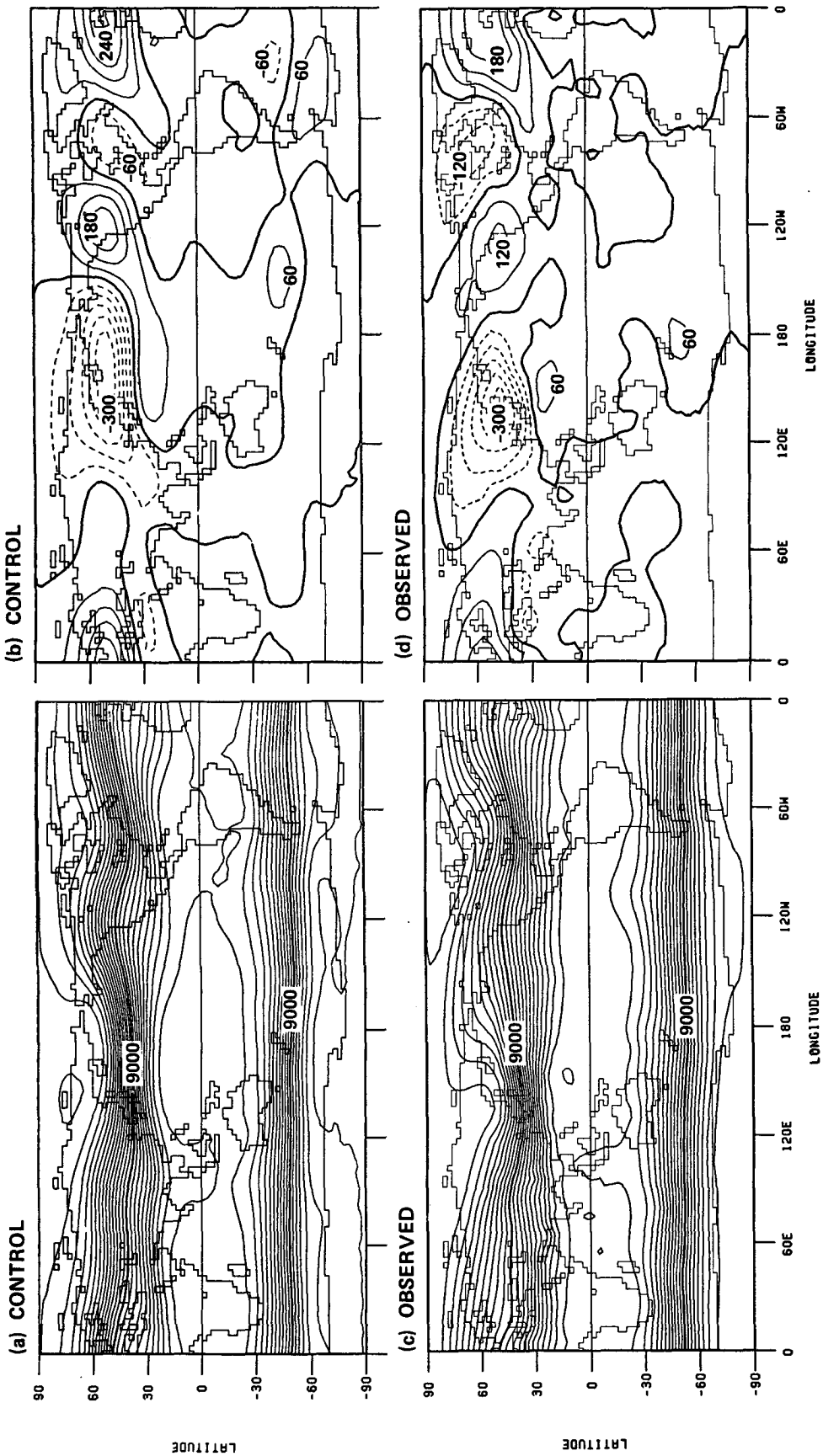

FIG. 2. Winter (December–February) means at 300 mb for (a) geopotential field (m) in the control experiment; (b) its deviation from zonal average; (c) corresponding observed field for (a); and (d) corresponding observed field for (b). Contour interval: 60 m. Thicker contour in (a) and (c) corresponds to 9000 m. Negative contours in (b) and (d) are dashed.

served climatology, taken from the Global Atmospheric Circulation Statistics, 1958–73, compiled by Oort (1983). Other simulated fields, such as precipitation, will be shown in subsequent sections.

a. Time mean fields

Winter means of simulated and observed geopotential fields and their deviation from the zonal average at 300 mb are given in Fig. 2. Inspection of this figure reveals that the model performance is generally good. There are, however, some important differences between simulated and observed fields. The simulated geopotential field over the north Pacific is more zonal. This reflects the weak vertical tilt of the simulated Aleutian Low. Correspondingly, geopotential gradients are stronger than observed over a zonally extended region. Further, gradients are too strong in the Southern Hemisphere midlatitudes. Removal of the zonal average clearly shows that the highs over western North America and Europe are well simulated. On the other hand, the trough over eastern North America is weaker than observed.

Winter means of simulated and observed wind fields at 300 mb are shown in Fig. 3. In the Northern Hemisphere the simulated field shows jet streams over Japan and the east coast of North America. Both the position and intensity of those jet streams compare favorably with observations. However, the jet over Japan extends further eastward than observed. In the Southern

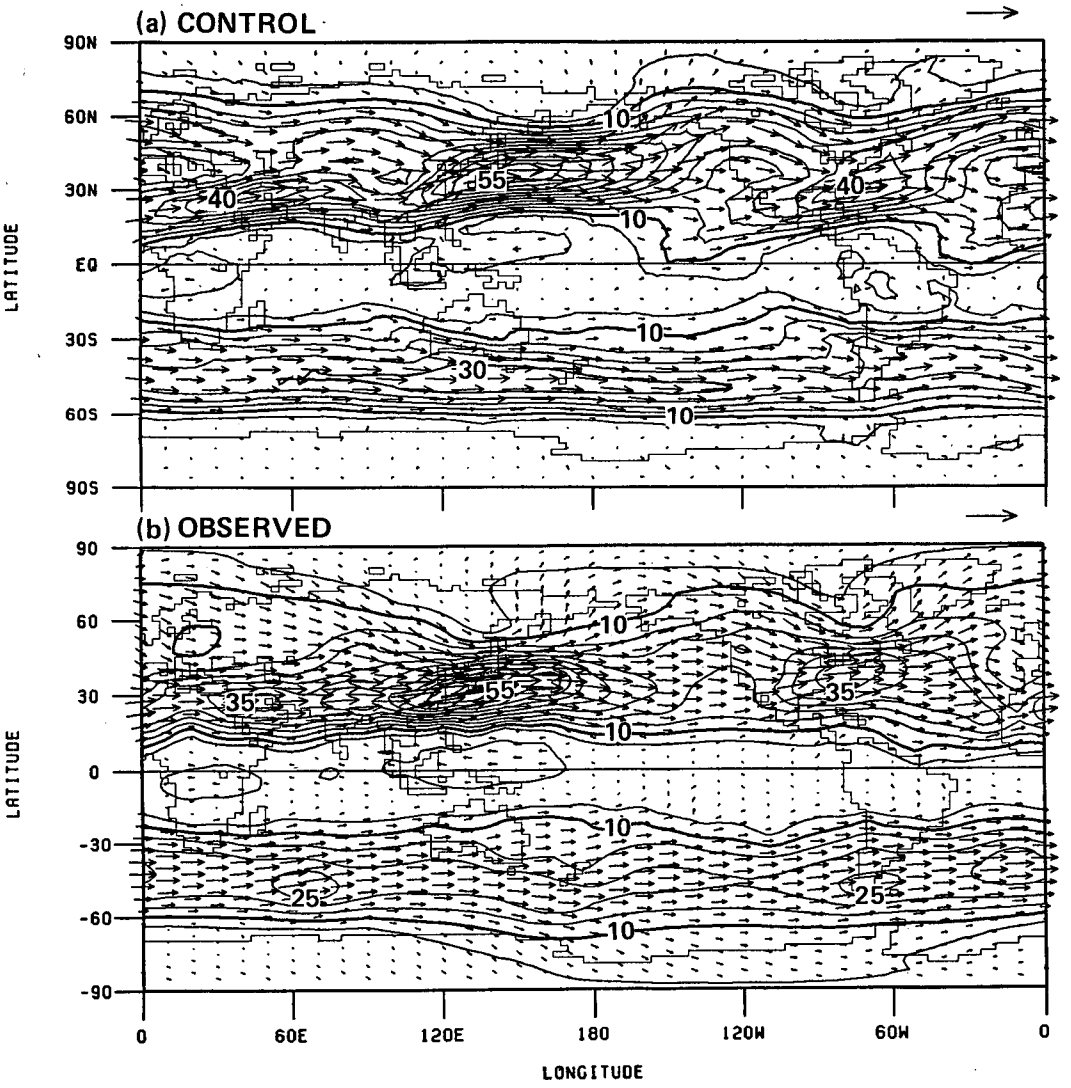

FIG. 3. Winter means of (a) wind fields (m s^{-1}) at 300 mb in the control experiment and (b) corresponding observed field. Reference arrow: 50 m s^{-1}. Contours represent wind speed. Contour interval: 5 m s^{-1}. Thicker contour corresponds to 10 m s^{-1}.

Hemisphere, midlatitude westerlies are generally overpredicted.

b. Temporal variances

Simulated and observed temporal variances of geopotential and wind for winter are shown in Figs. 4 and 5, respectively. It is immediately apparent that the model underpredicts these variances. Nevertheless, positions of local maxima in both fields are in qualitative agreement with the observations, particularly over the oceans. Local minima in geopotential variance over the continents of the Northern Hemisphere are not well simulated. Consequently, the simulated pattern of geopotential variance is more zonal than observed. The simulated wind variance has local minima over western North America and Siberia, as observed.

5. The tropical response to the SSTA

An expected direct effect of the SSTA is the enhancement of moist-convective instability in the tropics. This expectation is confirmed by Figs. 6a and 6b, which show the winter mean moist static energy in the PBL for the control and anomaly experiments, respectively. The region of large moist static energy, which is around the dateline in the control experiment, expands eastward in the anomaly experiment, covering almost the entire tropical Pacific. The contributions to the anomalous moist static energy by the anomalous dry static energy and latent heat are shown in Figs. 6c and 6d, respectively. Both contributions strongly resemble the SSTA pattern in Fig. 1, but the latter is about twice as large as the former.

The winter mean precipitation over the tropical Pa-

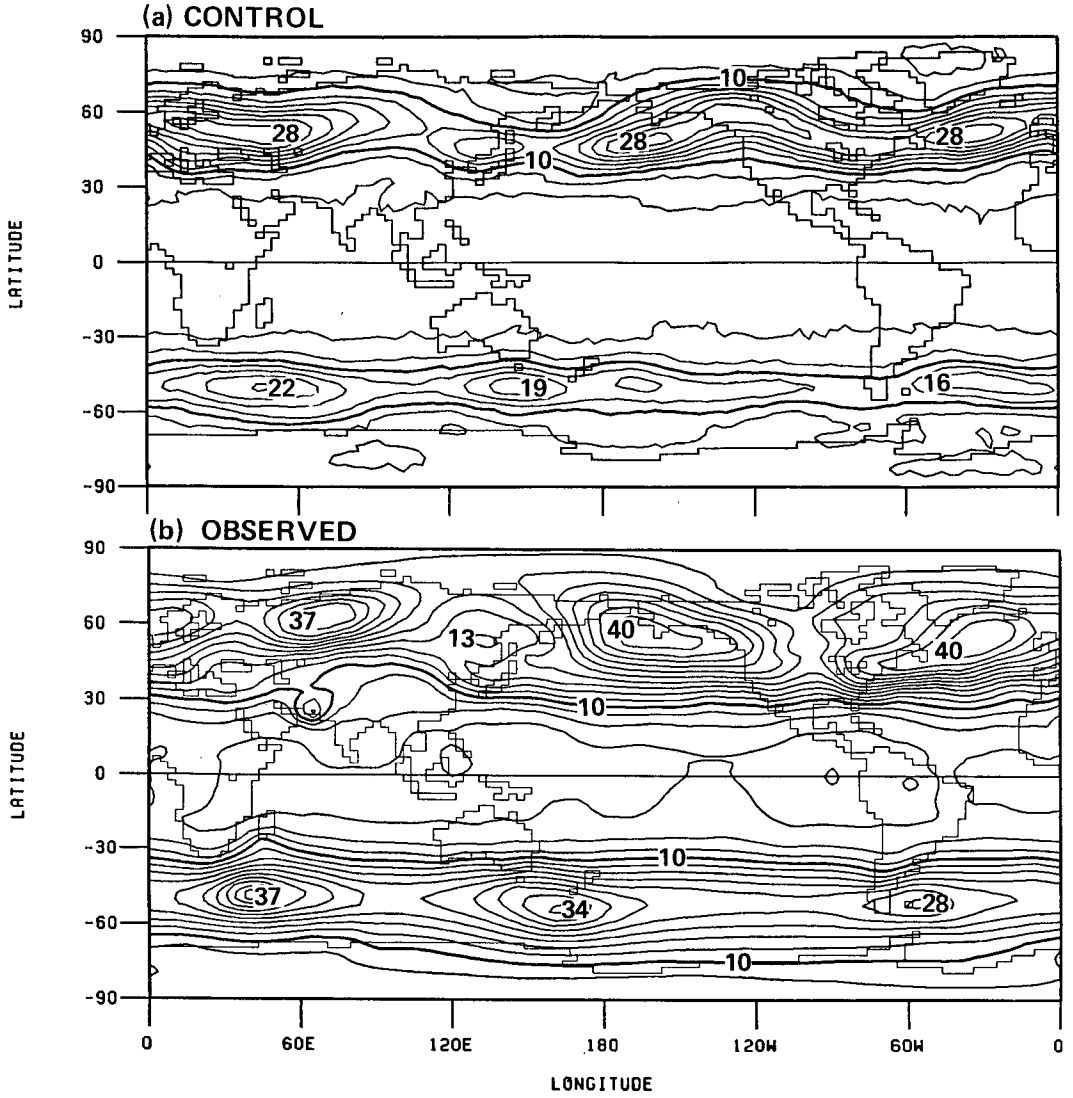

FIG. 4. (a) Geopotential variance (10^3 m^2) in the control experiment at 300 mb and (b) corresponding observed field. Contour interval: 3000 m^2. Thicker contour corresponds to 10^4 m^2.

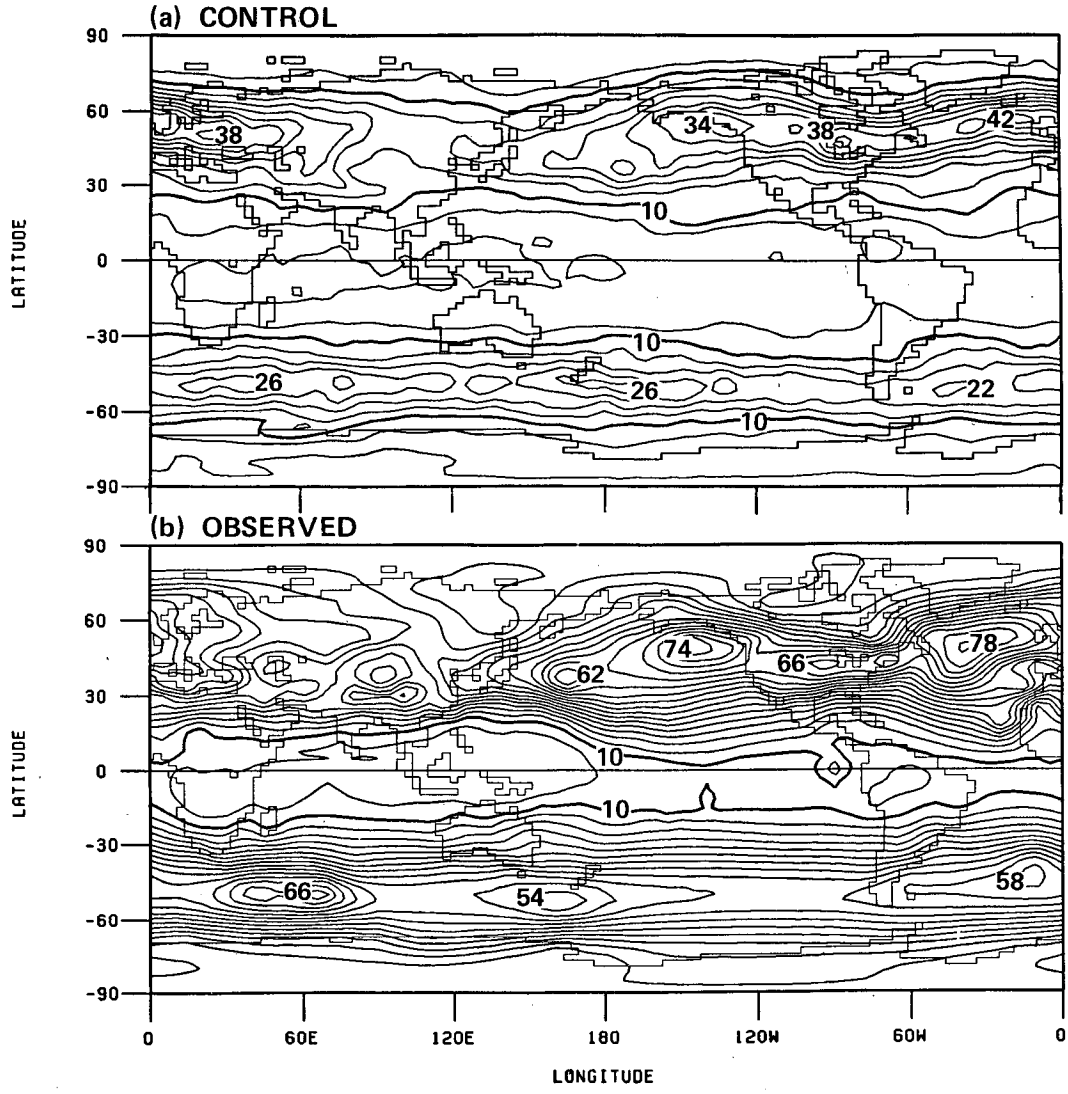

FIG. 5. As in Fig. 4, except for wind variances (10 $m^2 s^{-2}$). Contour interval: 40 $m^2 s^{-2}$. Thicker line corresponds to 100 $m^2 s^{-2}$.

cific for the control experiment and corresponding anomalous field are shown in Fig. 7. In the control experiment, precipitation is intense over an area that extends across the entire Pacific around 10°N. The maximum precipitation in this area appears around 170°W, 5°N. The South Pacific Convergence Zone (SPCZ) extends from there toward the southeast. Another area of localized intense precipitation, which is associated with the winter monsoon, is at the periphery of Australia and over New Guinea. The precipitation is also large over the Amazon Basin. It is weak in the southeastern Pacific, where SST is low, and over the subtropical high around 25°N. The anomalous field shows that precipitation is enhanced over the central and eastern equatorial Pacific and decreased over the northern and southern flanks of the large anomalous precipitation area. The decrease in precipitation in the trade wind region and over the eastern periphery of Australia is consistent with observations during El Niño years (Quiroz, 1983). In summary, the anomalous precipitation pattern is characterized by a southward extension of the dry zone centered around 25°N over the western and central Pacific, and by an intensification of the ITCZ rainband over the central and eastern Pacific.

Anomalous precipitation in the equatorial Pacific is associated with anomalous cumulus activity. Winter mean cumulus heating averaged over 10°S–10°N for the control experiment and corresponding anomalous field are shown in Fig. 8. In the control experiment, relative maxima of cumulus heating exist over the western and central Pacific. There are also maxima over the South American and African continents. The anomalous field shows significantly enhanced cumulus

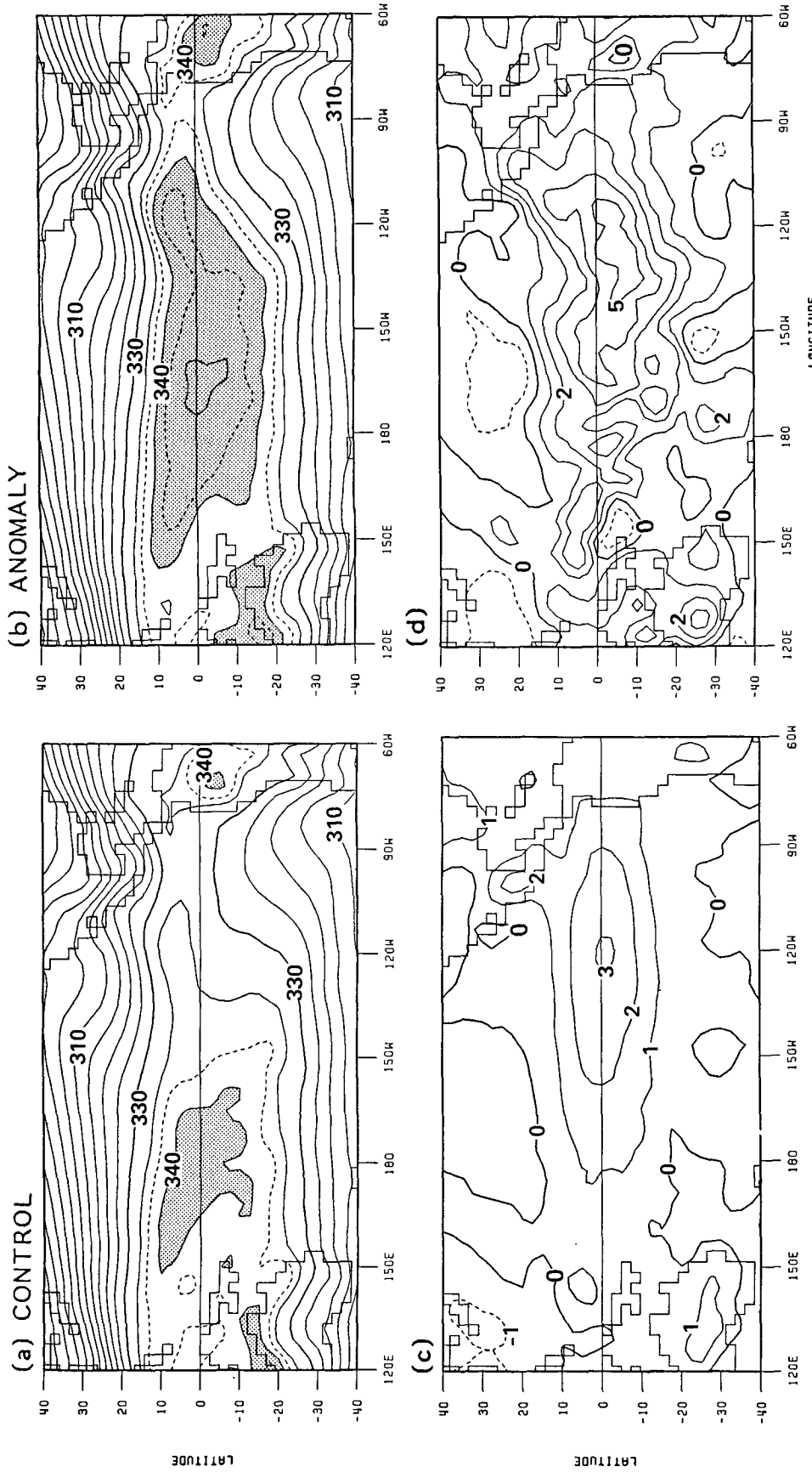

FIG. 6. The winter mean moist static energy (10^3 J kg^{-1}) in the PBL for (a) control and (b) anomaly. Contributions to the anomalous moist static energy by anomalous (c) dry static energy and (d) latent heat. For (a) and (b) the contour interval for solid contours is 5×10^3 J kg^{-1}. Thicker contour corresponds to 330×10^3 J kg^{-1}. For (c) and (d) the contour interval is 10^3 J kg^{-1} and negative contours are dashed.

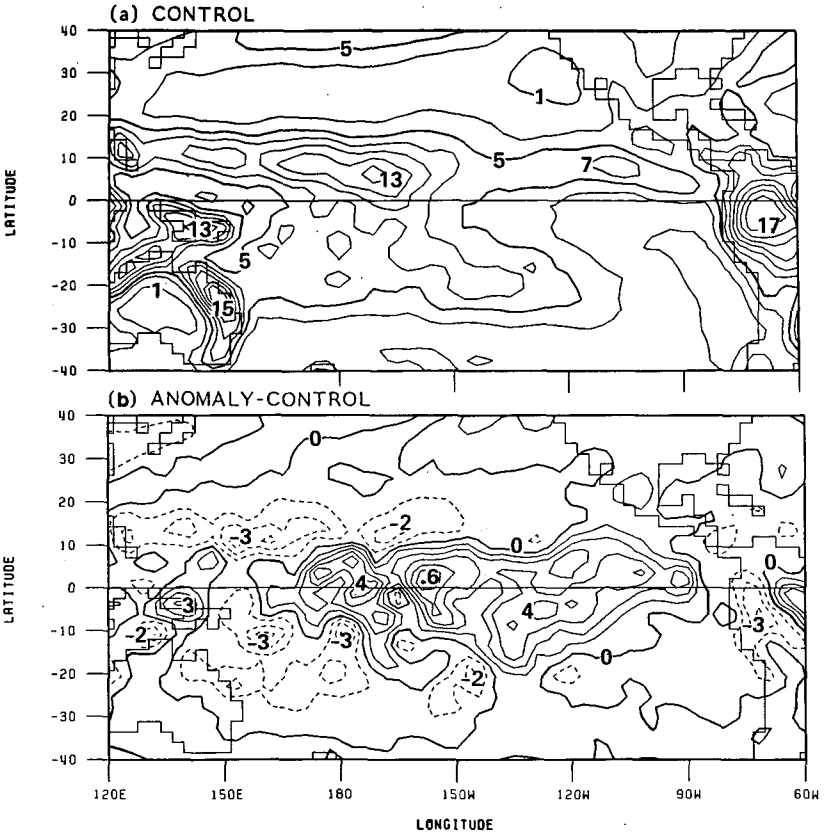

FIG. 7. The winter mean precipitation (mm day^{-1}) for (a) control, (b) anomaly − control. Contour interval: 2 mm day^{-1} for (a) and 1 mm day^{-1} for (b). Negative contours are dashed. Thicker contour in (a) corresponds to 5 mm day^{-1}.

heating over the Pacific around and towards the east of the dateline. This anomalous cumulus heating shows three maxima. From east to west, the first maximum is near the location of maximum SSTA (120°W). The second and third maxima are near 150°W and near the dateline, respectively. The anomalous cumulus heating over the Pacific is deeper towards the west.

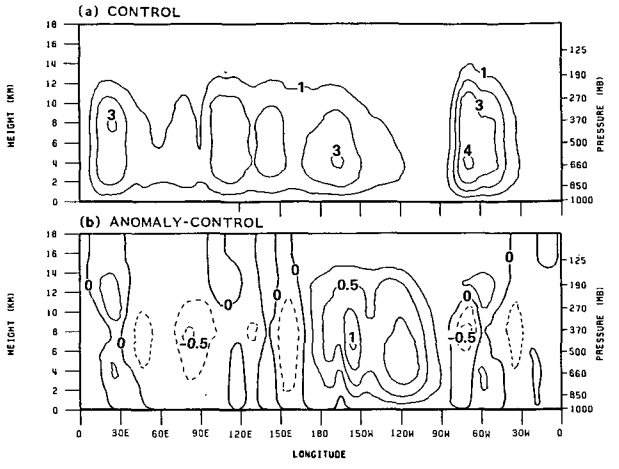

FIG. 8. Longitude–height cross section of the winter mean cumulus heating (K day^{-1}) in the latitude band 10°S–10°N for (a) control, (b) anomaly − control. Contour interval: 1 K day^{-1} for (a) and 0.25 K day^{-1} for (b). Negative contours are dashed.

The winter mean evaporation for the control experiment and corresponding anomalous field are shown in Fig. 9. In the control experiment, the spatial distribution of evaporation is generally smoother than that of precipitation. Nevertheless, there are strong local maxima along the west coast of Central America and over the Gulf of Mexico. These maxima are due to dry PBL winds blowing southwest from North America. An area of large evaporation between the subtropical highs extends from the western Pacific around 15°N to the eastern Pacific around 20°S. There is also large evaporation over the eastern periphery of Australia. The anomalous evaporation has well-organized maxima over the equatorial eastern Pacific and less-organized maxima in the equatorial western Pacific.

It is clear from Figs. 7b and 9b that the anomalous precipitation is not generally balanced by the anomalous evaporation. This confirms that anomalies in moisture transport, rather than in situ evaporation, are generally responsible for the anomalous precipitation

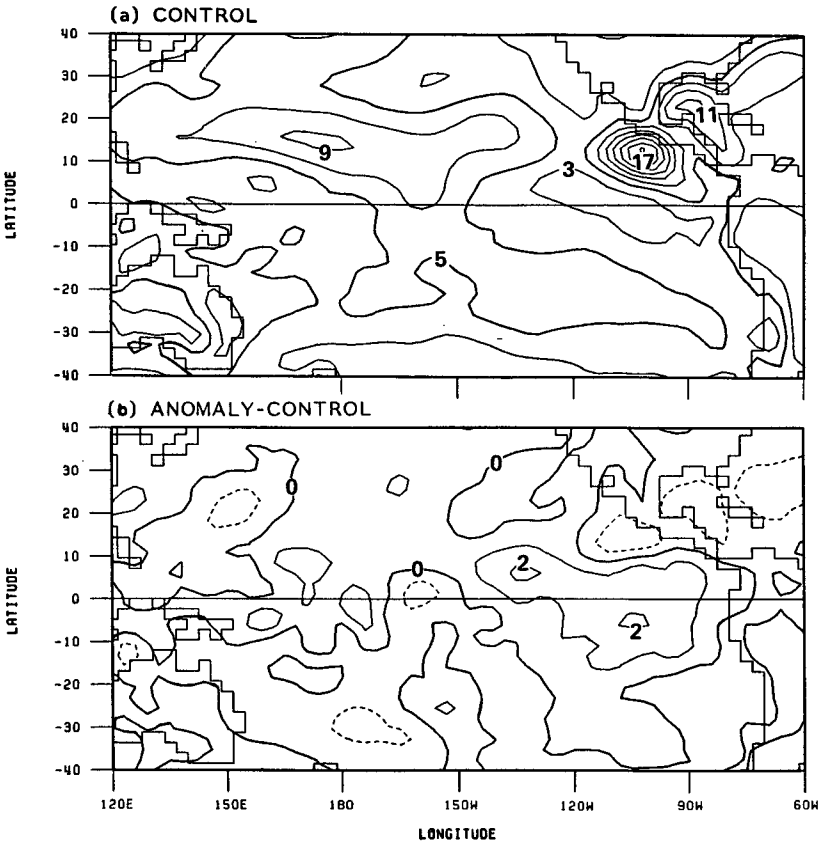

FIG. 9. As in Fig. 7, except for evaporation.

as found by previous authors (Cornejo-Garrido and Stone, 1977; Julian and Chervin, 1978; Shukla and Wallace, 1983). The anomalous evaporation is a significant contributor to the anomalous precipitation only where it is maximum.

We now focus on the anomalous moisture flux and its convergence. For this purpose, we consider the PBL and the free atmosphere separately, since they are affected by different physical processes. Such a separation can be easily accomplished for the UCLA GCM, in which the variable-depth PBL is the lowest model layer. The expressions for the moisture flux in the PBL and the free atmosphere are, respectively,

$$(\mathbf{MF})_{\mathrm{PBL}} \equiv \frac{1}{g}\int_{p_B}^{p_S} q\mathbf{v}\,dp, \tag{1}$$

$$(\mathbf{MF})_{\mathrm{FA}} \equiv \frac{1}{g}\int_{p_T}^{p_B} q\mathbf{v}\,dp, \tag{2}$$

where $\mathbf{v}$ is horizontal velocity; q is mixing ratio of water vapor; p is pressure; p_T, p_B and p_S are the pressures at the model's top (51.8 mb), the PBL top and the earth's surface, respectively; and g is the acceleration due to gravity.

The winter mean anomalous moisture flux in the PBL and the free atmosphere and their convergence are shown in Figs. 10 and 11, respectively. The anomalous flux is generally smaller in the PBL than in the free atmosphere, as expected from the shallowness of the PBL. However, the anomalous moisture flux convergence in the PBL and that in the free atmosphere have comparable magnitude with quite different geographical distribution.

In the PBL, there is intense anomalous flux over the western Pacific. This anomalous flux is equatorward around 10°N and eastward around the equator. It is associated with increased local Hadley circulation and decreased Walker circulation. Convergence of this anomalous flux north of the equator is organized in a zonal belt with a maximum over the area of large anomalous precipitation around 150°W (see Fig. 7b), while convergence just south of the equator is less organized. There is also intense northwestward anomalous flux over the eastern Pacific south of the equator, which is strongly convergent over the area of large anomalous precipitation south of the maximum SSTA (see Fig. 7b).

In the free atmosphere, intense anomalous flux over the western Pacific has a pattern similar to that in the

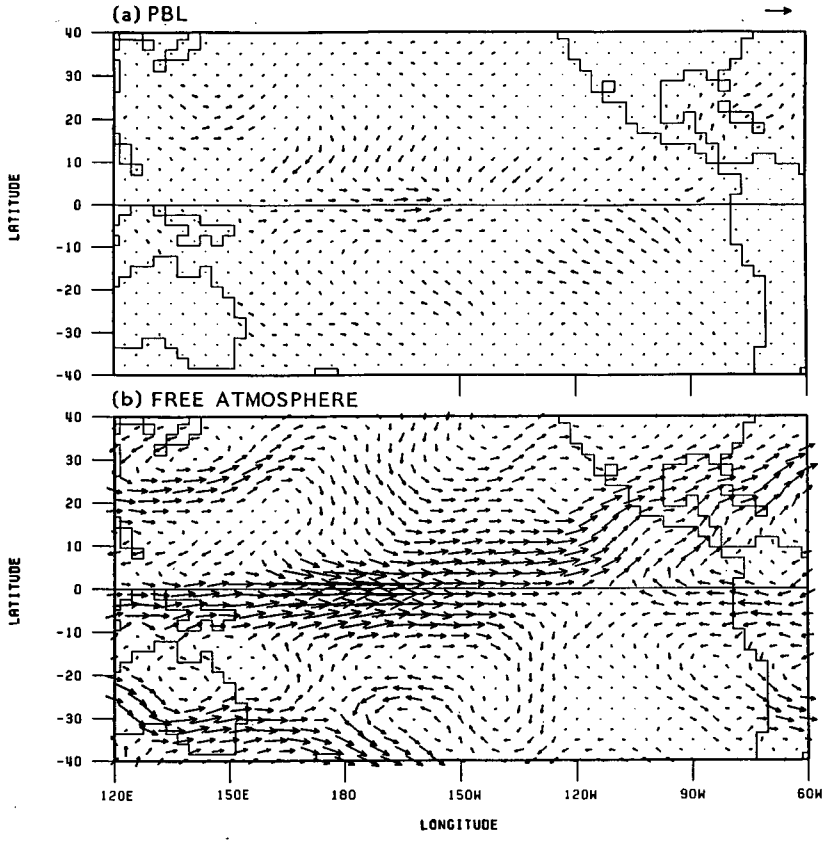

FIG. 10. The winter mean anomalous moisture flux for (a) PBL and (b) free atmosphere. Reference arrow: 7.5×10^6 m mm day^{-1}.

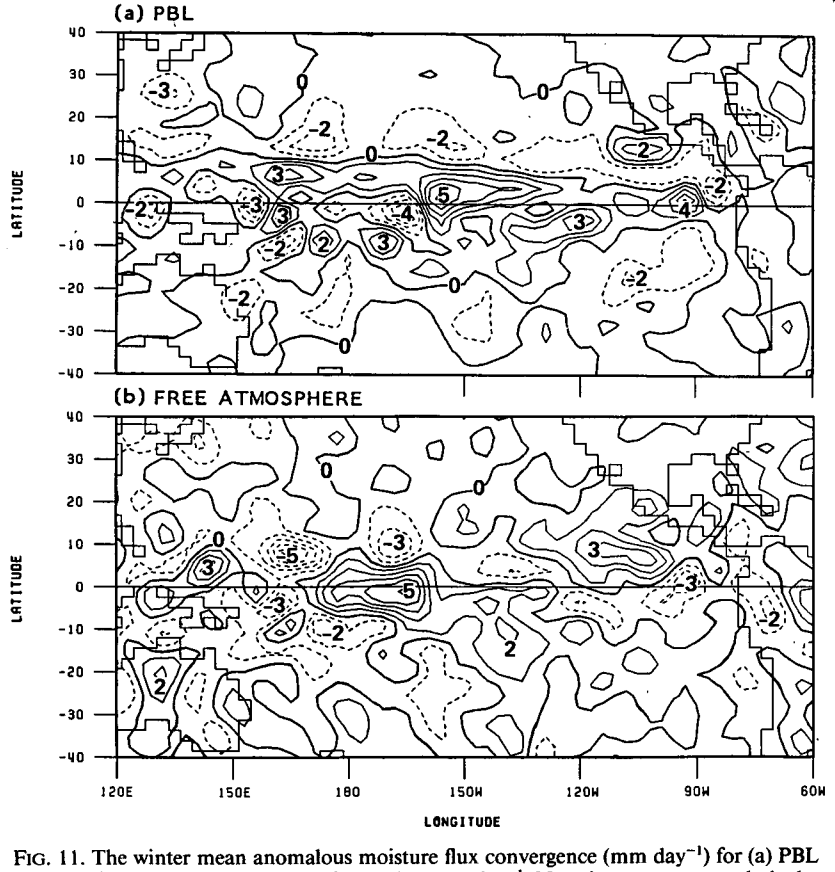

FIG. 11. The winter mean anomalous moisture flux convergence (mm day^{-1}) for (a) PBL and (b) free atmosphere. Contour interval: 1 mm day^{-1}. Negative contours are dashed.

PBL, but with larger magnitude. The anomalous flux is associated with increased local Hadley circulation and decreased Walker circulation. It is strongly convergent over the area of large anomalous precipitation east of the dateline near the equator (see Fig. 7b) and weakly convergent over the SPCZ. There is also intense anomalous flux over the eastern Pacific, which is westward from South America south of the equator, and eastward to northeastward north of the equator. The latter, which is associated with decreased trade winds, is convergent over the area of large anomalous precipitation northeast of the maximum SSTA (see Fig. 7b).

The moisture flux potential for the PBL and the free atmosphere (Q_{PBL} and Q_{FA}, respectively) are defined by the following relations:

$$\nabla^2 Q_{PBL} = \nabla(\mathbf{MF})_{PBL}, \tag{3}$$

$$\nabla^2 Q_{FA} = \nabla(\mathbf{MF})_{FA}. \tag{4}$$

The winter means of anomalies in Q_{PBL} and Q_{FA} and in divergent components of $(\mathbf{MF})_{PBL}$ and $(\mathbf{MF})_{FA}$, are shown in Fig. 12. The anomalous moisture flux potential in the PBL is highly localized over the equatorial Pacific whereas that in the free atmosphere has a global structure. In agreement with previous results, the divergent component of the anomalous moisture flux in the PBL is larger over the central Pacific north of the equator and over the eastern Pacific south of the equator while that in the free atmosphere is larger near the dateline over the equator. Interestingly, however,

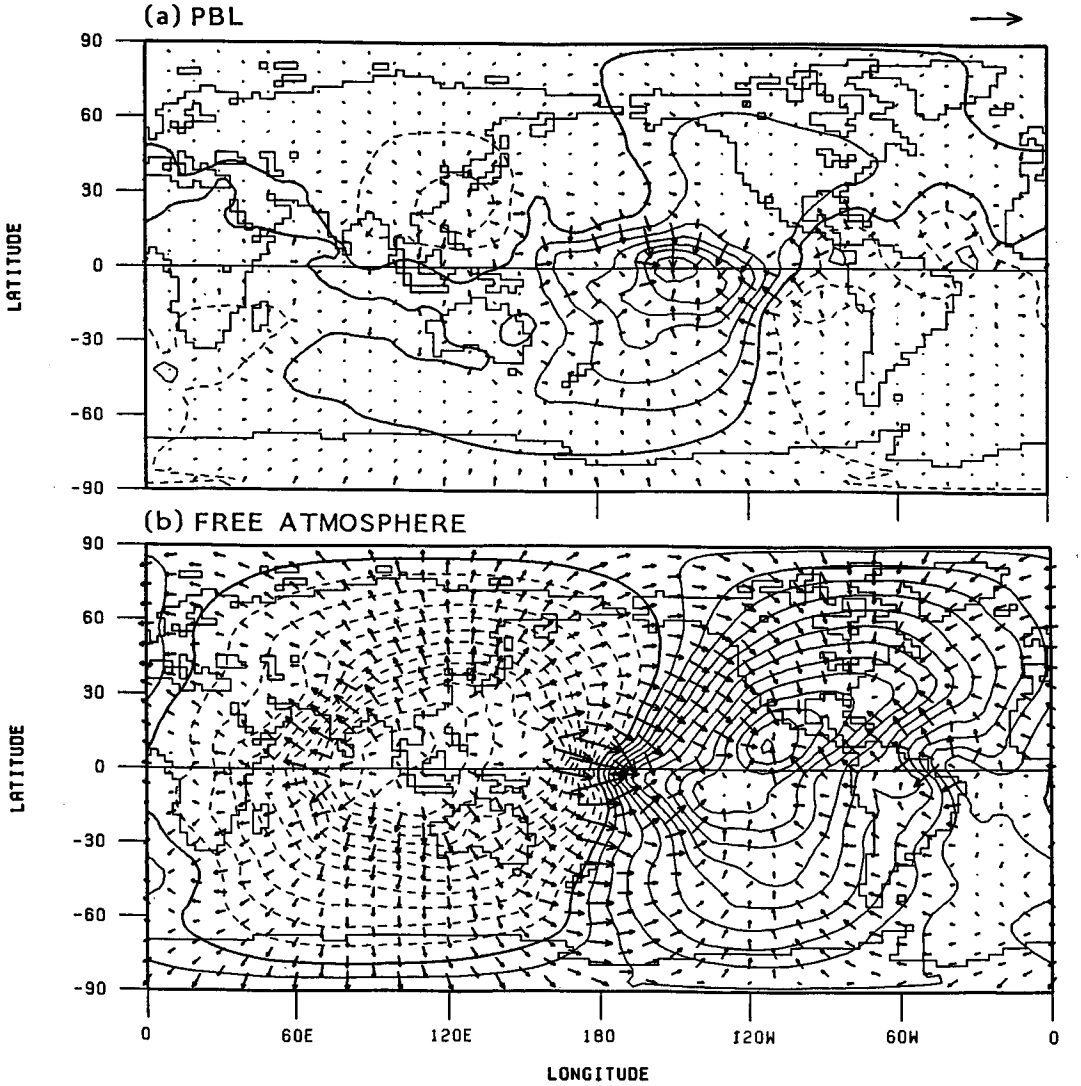

FIG. 12. The winter mean anomalous moisture flux potential and divergent component of the anomalous moisture flux for (a) PBL and (b) free atmosphere. Contour interval: 5×10^{11} m^2 mm day^{-1}. Reference arrow: 3×10^6 m mm day^{-1}.

anomalous flux in the free atmosphere is also large over extended areas far away from the eastern Pacific.

6. The global response to the SSTA

The winter mean geopotential anomalies obtained as a response to the SSTA are shown in Fig. 13 for 300 and 700 mb. In the tropics they are generally positive at all levels. The maximum geopotential anomaly at 300 mb is over the eastern equatorial Pacific. The anomaly in geopotential thickness between 300 and 700 mb is maximum over the eastern equatorial Pacific where convection is enhanced. The sea-level pressure anomaly along the equator (not shown) has a maximum around 80°E and a minimum around 120°W, consistent with the observed relationship between the phase of the Southern Oscillation and El Niño events (Bjerknes, 1969; Angell, 1981; Horel and Wallace, 1981).

In middle and high latitudes, the response shown in Fig. 13 has an equivalent-barotropic structure as pointed out by many authors (e.g., Wallace and Gutzler, 1981). Nevertheless, the responses in the Southern and Northern Hemispheres are significantly different. In the Southern Hemisphere, the response is predominantly zonal, with negative anomalies between 30° and 60°S except over the eastern South Pacific. This agrees with observations during El Niño years (Karoly, personal communication). In the Northern Hemisphere, the response is more variable in the zonal di-

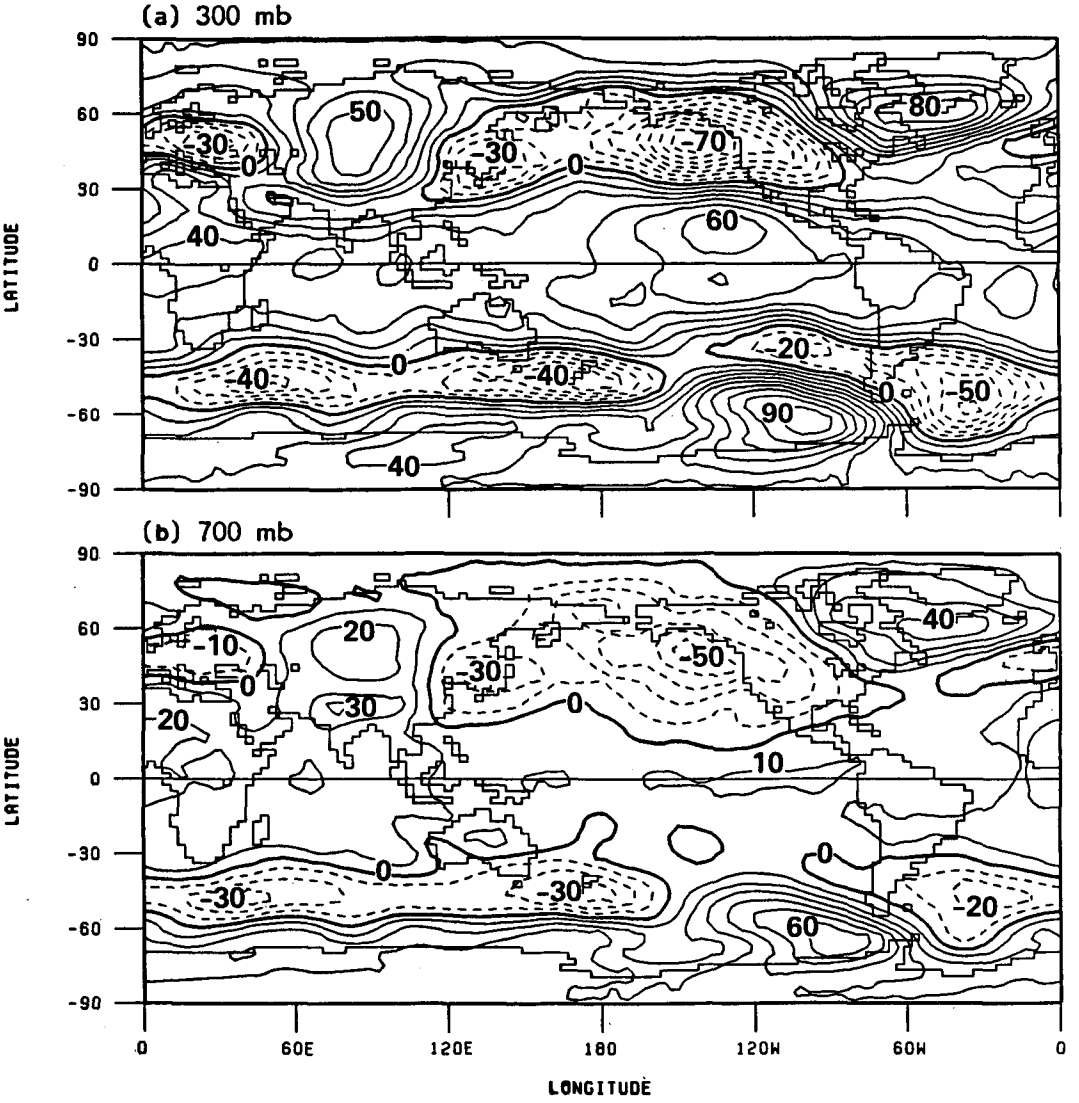

FIG. 13. The winter mean geopotential height anomaly (m) at (a) 300 mb and (b) 700 mb. Contour interval: 10 m. Negative contours are dashed.

rection with negative anomalies from Japan to western North America and over Europe, and positive anomalies over eastern Greenland and central Eurasian continent.

The response in the Northern Hemisphere resembles the PNA (Pacific–North American) pattern described by Wallace and Gutzler (1981). However, the pattern of the response is more elongated in the zonal direction than the PNA, particularly from the western Pacific to eastern Atlantic. Such an elongation in the zonal direction is similar to that obtained in the model climatology, as discussed in section 3. The eastward extension over North America of the region with negative anomalies may be at least partially due to the lack of envelope orography effects (see Palmer and Mansfield, 1986a). Closer analogs to the PNA pattern are obtained in monthly means (not shown) for February and, to a lesser extent, for December. Locations of high and low centers of the latter pattern are, however, displaced eastward relative to their counterparts in the former. Analyses of daily fields reveal the absence of positive persistent anomalies over the north Pacific in both control and anomaly experiments (Horel and Mechoso, personal communication).

The winter mean anomalous streamfunction and rotational component of the wind at 300 and 850 mb are shown in Fig. 14. At 300 mb, there are anomalous westerlies in the subtropics over the Pacific and anom-

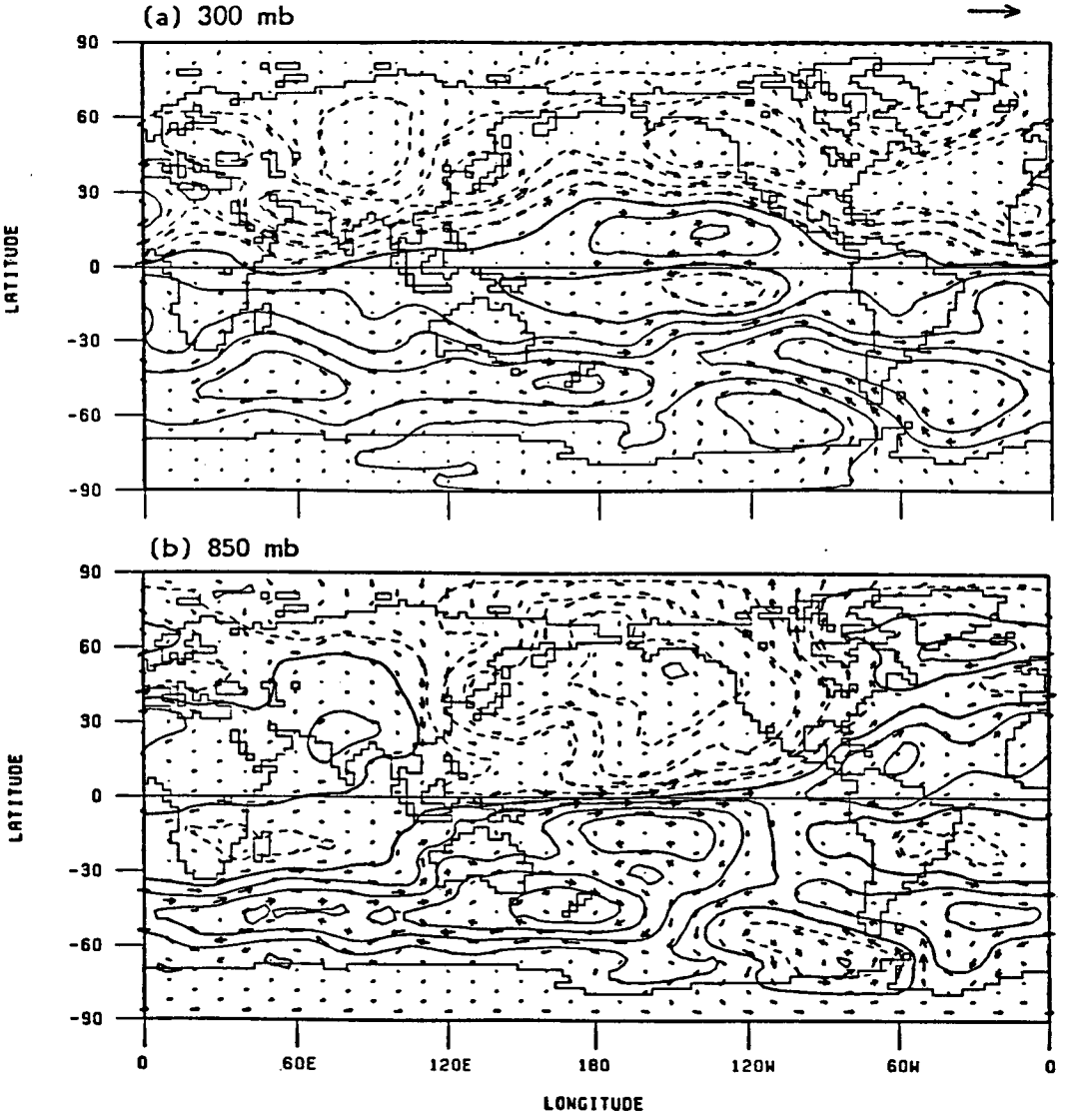

FIG. 14. The winter mean anomalous streamfunction and rotational wind at (a) 300 mb and (b) 850 mb. Contour interval: 2.5×10^6 m^2 s^{-1} for (a) and 1.25×10^6 for (b). Reference arrow: 20 m s^{-1} for (a) and 10 m s^{-1} for (b).

alous easterlies in the eastern equatorial Pacific. The anomalous easterlies are associated with a pair of anticyclones to the northwest and southwest of the maximum SSTA. At 850 mb there are anomalous westerlies over most of the equatorial Pacific. East of the dateline, these anomalous westerlies are due to weaker easterlies in the anomaly experiment than in the control. West of the dateline, they are due to a flow reversal from easterly in the control experiment to westerly in the anomaly. Figure 14b also shows the intensification of the Aleutian Low in the anomaly experiment. These results are similar to those found in other GCM experiments for the Northern Hemisphere winter (Blackmon et al., 1983; Tokioka et al., 1985b) and the Northern Hemisphere summer (Keshavamurty, 1982; Tokioka et al., 1985a), as well as in observational studies (Horel and Wallace, 1981).

The winter mean anomalous velocity potential and divergent component of the wind at 300 and 850 mb are shown in Fig. 15. The anomalous velocity potential has a wavenumber 1 pattern at both levels, with centers of divergence (convergence) over the maximum SSTA and convergence (divergence) over the maritime continent. This anomalous pattern differs markedly from those in the control and anomaly experiments, which are dominated by centers over the central and western equatorial Pacific. Figure 15 shows an anomalous east–west circulation (reverse Walker circulation) between

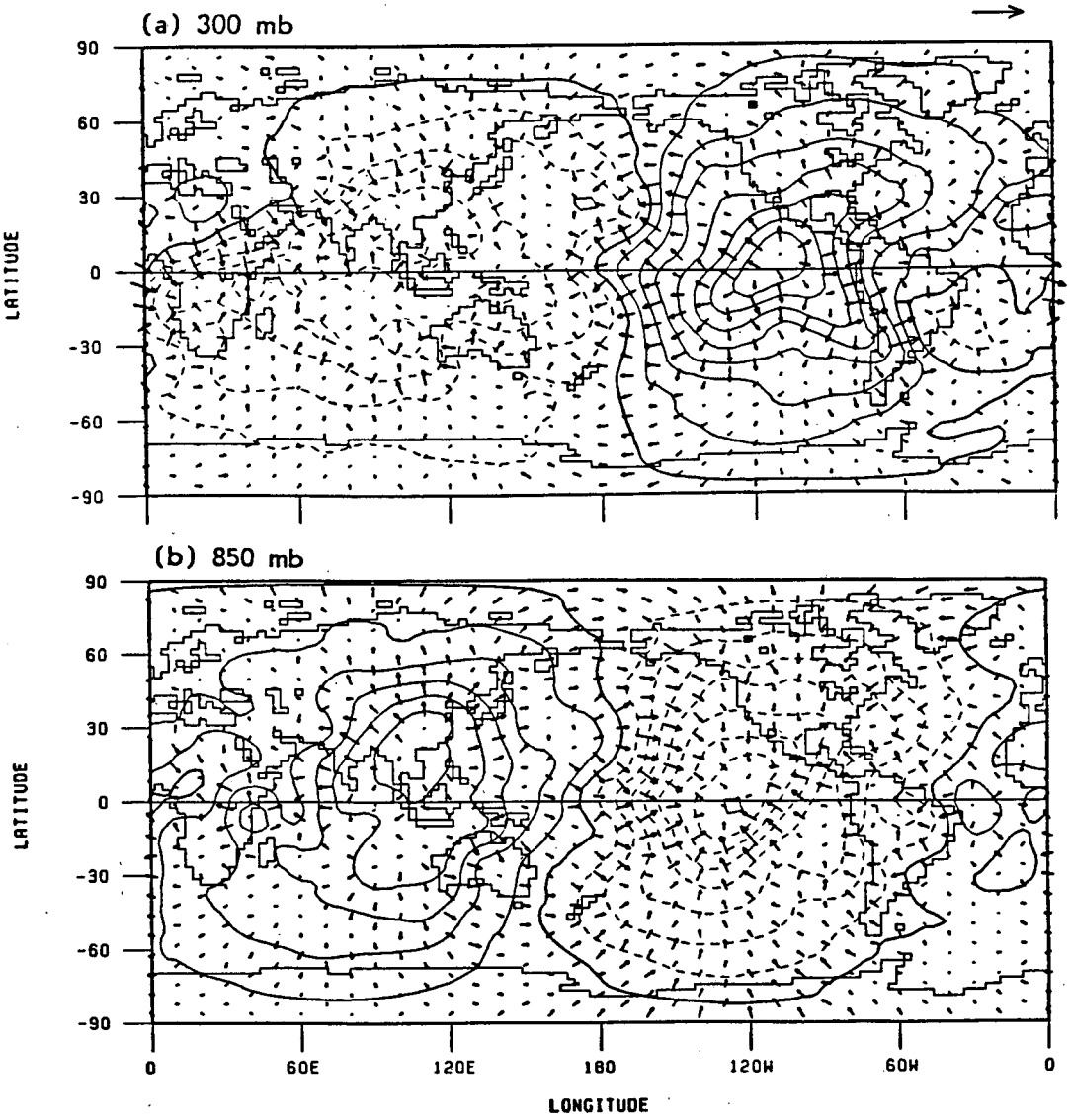

FIG. 15. As in Fig. 14, except for velocity potential and divergent component of the wind. Contour interval: 0.5×10^6 m^2 s^{-1}. Reference arrow: 2.5 m s^{-1}.

the eastern Pacific and the maritime continent, and the strengthening of local Hadley circulation over the Pacific.

An insight into the activity of the transients can be gained by using the space–time spectral analysis technique (Hayashi, 1971). We applied this technique to the October–February time series of meridional velocity for both the control and anomaly experiments. The results for 50°N at 300 mb are shown in Fig. 16. Most of the variance is due to eastward-moving waves in both experiments, but the distributions of the variance are significantly different. The maximum contribution to the variance in the control experiment is from eastward-moving wavenumber 4 with a period of about 10 days. On the other hand, the maximum contribution in the anomaly experiment is from eastward-moving wavenumber 6 with a period of about 4 days. Furthermore, the power in the low-wavenumber and low-frequency range is smaller in the anomaly experiment than in the control.

It appears, therefore, that the SSTA results in increased activity of midlatitude synoptic-scale medium-frequency transients. The space–time spectral analysis of observed geopotential height for 50°N at 500 mb performed by Fraedrich and Böttger (1978) for five winter seasons (1972–77) shows that a similar increase occurred during the El Niño winters of 1972/73 and 1976/77.

To determine preferred geographical locations of increase in the synoptic-scale medium-frequency transients, we applied Blackmon's (1976) medium-pass filter to the simulated fields. This filter retains periods between 2.5 and 6 days. The distributions of root-mean-square (rms) medium-pass filtered meridional velocity at 300 mb are shown in Figs. 17a and 17b for the control and anomaly experiments, respectively. In the Northern Hemisphere, the major regions of increased rms values are over North America and north of the British Isles. In the Southern Hemisphere, the region of increased rms values shows small variations in longitude.

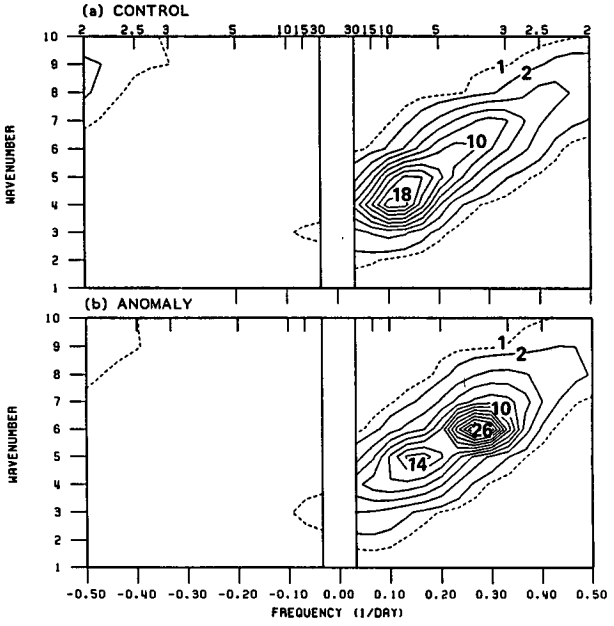

FIG. 16. Spectral density of the meridional velocity (10 $m^2 s^{-2}$ day) for 50°N at 300 mb for (a) control and (b) anomaly. Contour interval: 20 $m^2 s^{-2}$ day.

The time evolution after 22 August of the medium-pass filtered transient eddy kinetic energy (KE) at 300 mb averaged over 30° to 90°N for the control and anomaly experiments is shown in Fig. 18. The increasing trend of KE during the first three months is due to the seasonal march from early to late fall in the Northern Hemisphere. In both the control and anomaly experiments, KE shows a rather similar behavior after the end of December. However, KE is significantly larger in the anomaly than in the control experiment from the end of November to the end of December. This intensification of KE changes the transient-active season from the late winter in the control experiment to the entire winter in the anomaly experiment. Such an extended activity of the medium-pass filtered eddies is responsible for their spectral peak in the anomaly experiment.

To further look into the characteristics of the transient eddy activity, we used the extended Eliassen–Palm (EEP) flux (Simmons et al., 1983; Hoskins et al., 1983). The EEP flux vector is a three-dimensional vector defined by

$$\mathbf{EEP} \equiv (\mathbf{E}, f_0 \overline{v'\theta'}/\Theta_p), \tag{5}$$

where f_0 is the Coriolis parameter, θ is potential temperature, Θ is a standard distribution of θ, and $\mathbf{E}$ is a horizontal vector defined by

$$\mathbf{E} \equiv -(\overline{u'^2 - v'^2}, \overline{u'v'}). \tag{6}$$

In expressions (5) and (6), overbars denote time average and primes denote deviation from time average. Arrows in Fig. 19 show $\mathbf{E}$ for both low-pass ($\mathbf{E}_L$) and medium-pass ($\mathbf{E}_M$) filtered eddies during the winter at 300 mb for both control and anomaly experiments. We again used Blackmon's (1976) low-pass filter, which retains periods larger than 10 days.

The low-pass eddies of the control experiment in the jet exit regions over the Pacific and Atlantic are zonally elongated ($\overline{u'^2} > \overline{v'^2}$) with $\mathbf{E}_L$ mostly opposite to the mean zonal flow gradient. These features are similar to those observed by Hoskins et al. (1983) for the "low-pass" eddies (eddies with periods greater than 10 days) at 250 mb during the 1979–80 winter. The $\mathbf{E}_L$ of the anomaly experiment is generally similar to that in the control experiment, but its magnitude is larger in the southern flank of the jet axis. On the other hand, the medium-pass eddies of the control experiment in the jet exit regions are meridionally elongated ($\overline{v'^2} > \overline{u'^2}$)

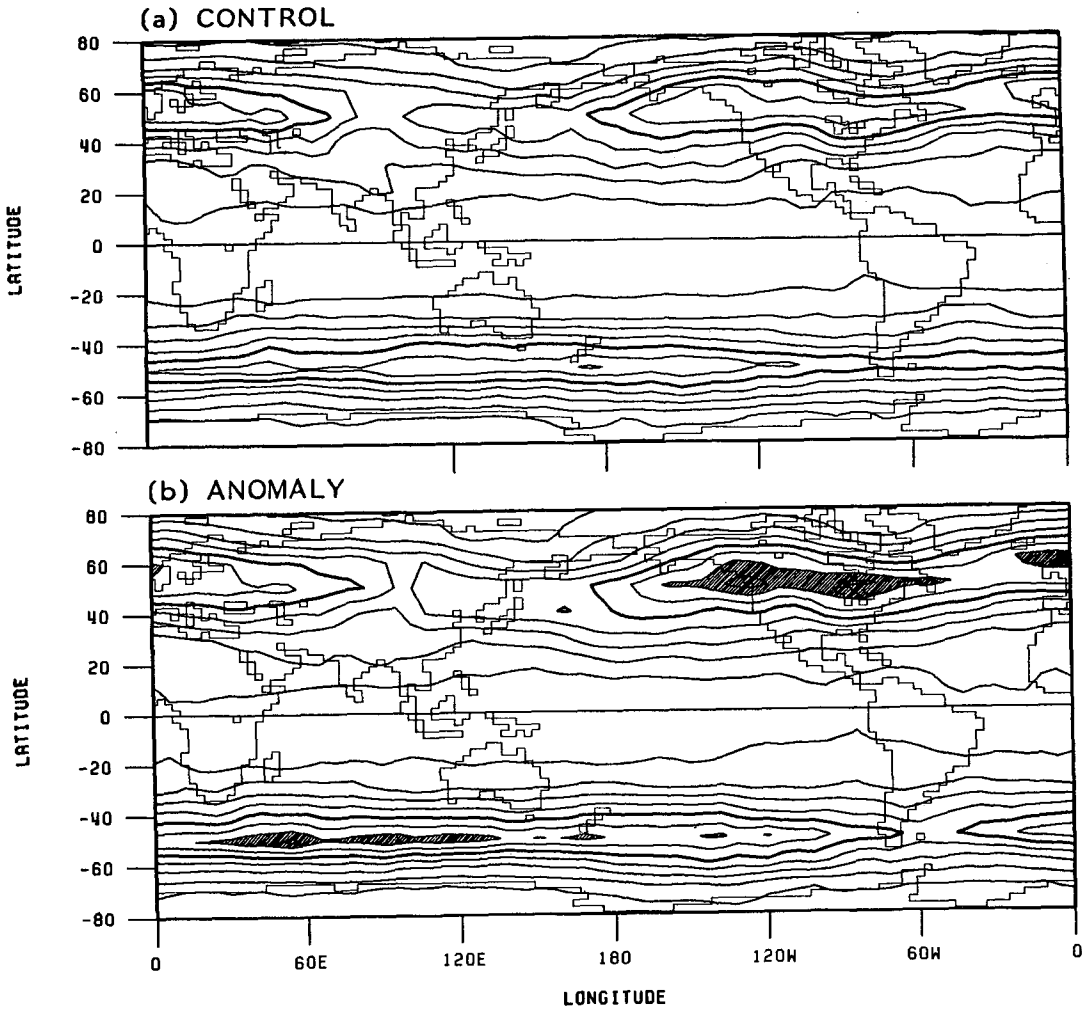

FIG. 17. Rms of medium-pass filtered meridional velocity (m s^{-1}) at 300 mb for (a) control and (b) anomaly. Contour interval: 1 m s^{-1}. Thicker contour corresponds to: 6 m s^{-1}. Values greater than 8 m s^{-1} are shaded.

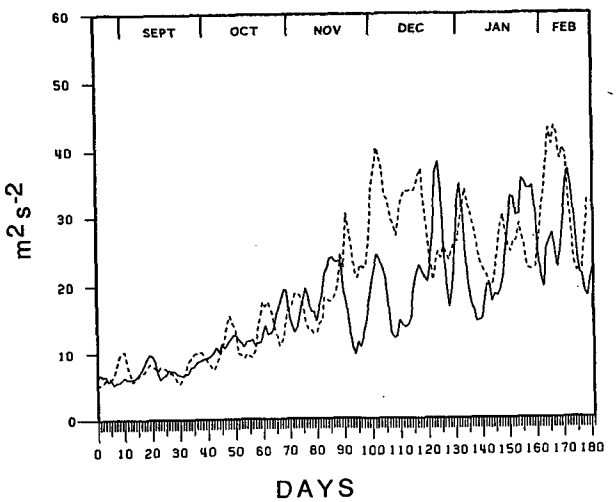

FIG. 18. Time evolution of kinetic energy for medium-pass filtered eddies at 300 mb averaged over 30°N–90°N for control (solid line) and anomaly (dashed line).

with $\mathbf{E}_M$ mostly along the mean zonal flow gradient. A similar feature is also observed by Hoskins et al., (1983) for the "high-pass" eddies (eddies with periods shorter than 10 days) at 250 mb during the 1979–80 winter. Also $\mathbf{E}_M$ of the anomaly experiment is similar to that in the control experiment, but its magnitude is larger, especially over the eastern Pacific, North America and the eastern Atlantic.

The barotropic conversion terms in the eddy kinetic energy (KE) equation are given by

$$\frac{1}{a}(\overline{v'^2}-\overline{u'^2})\left(\frac{1}{\cos\phi}\frac{\partial\bar{u}}{\partial\lambda}-\bar{v}\tan\phi\right) -\frac{1}{a}\overline{u'v'}\left(\cos\phi\frac{\partial}{\partial\phi}\left(\frac{\bar{u}}{\cos\phi}\right)+\frac{1}{\cos\phi}\frac{\partial\bar{v}}{\partial\lambda}\right)\approx\mathbf{E}\cdot\nabla\bar{u}, \quad (7)$$

where ϕ is latitude and λ is longitude. The values corresponding to the left-hand side of (7) are shown for low-pass and medium-pass eddies in Fig. 20. For low-

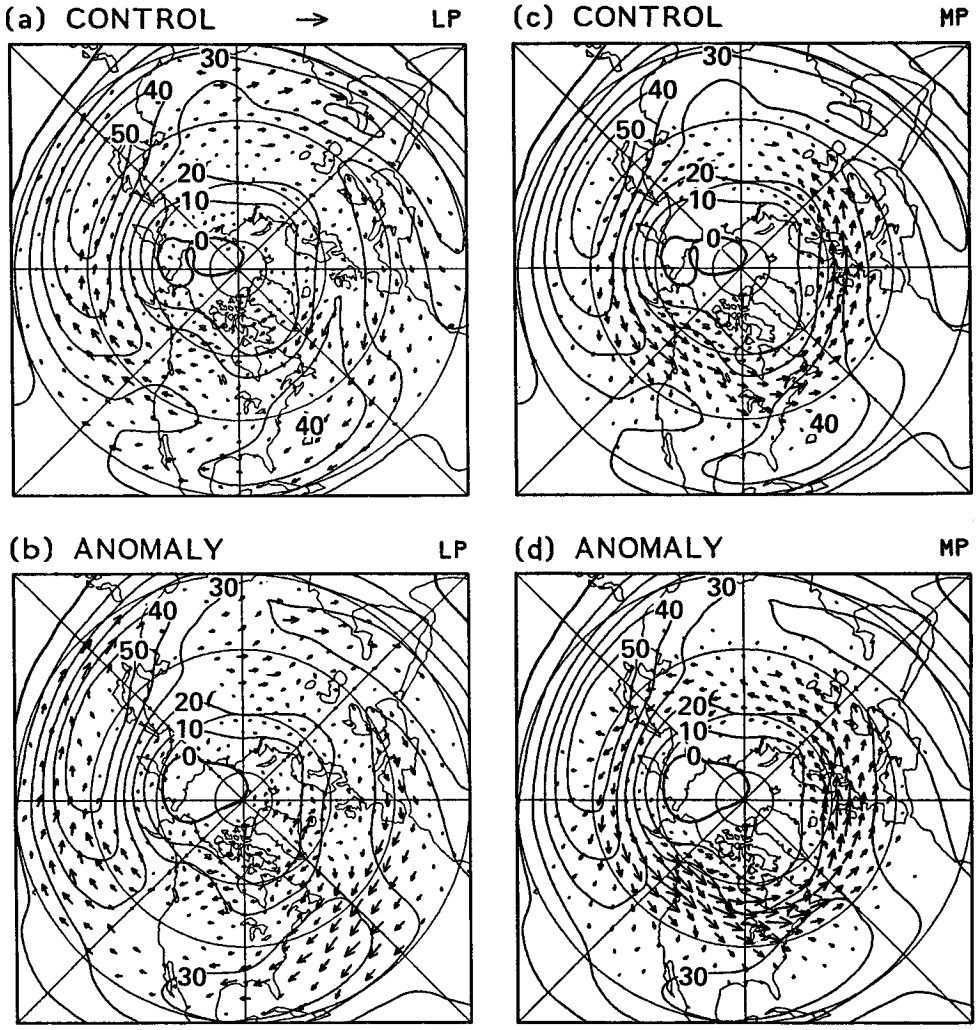

FIG. 19. *E*-flux vectors and contours of zonal wind (m s^{-1}) at 300 mb for low-pass eddies in (a) control, (b) anomaly, and medium-pass eddies in (c) control, (d) anomaly. Reference arrow: 100 m^2 s^{-2}. Contour interval: 10 m s^{-1}.

pass eddies, there are stronger positive values in the anomaly than in the control experiment for the southern flank of the jets over the Pacific and Atlantic Oceans, as the local KE tends to increase barotropically. For medium-pass eddies, there are stronger negative values in the anomaly than in the control experiment for the jet exit regions, particularly over the Pacific Ocean, as the local KE tends to decrease barotropically.

The vertical component of the EEP flux vector defined in (5) is proportional to the northward eddy heat flux. This is shown in Fig. 21 for the medium-pass eddies at 700 mb in both control and anomaly experiments. A comparison between Figs. 20 and 21 reveals that the local KE of these eddies tends to increase baroclinically rather than through the barotropic conversions given by (7). Furthermore, the larger northward heat flux by the medium-pass eddies in the anomaly experiment reveals that the increase in the activity of the synoptic-scale medium-frequency transients in midlatitudes is associated with the enhancement of baroclinic processes.

7. Summary and conclusions

We have studied the atmospheric response to a SSTA over the equatorial eastern Pacific using the high-resolution 9-layer version of the UCLA GCM. Two simulations over seasons, one with prescribed climatological time-varying SST and the other with the SSTA superimposed, were compared for the Northern Hemisphere winter season.

For the tropics, we have confirmed that the SSTA results in anomalous precipitation, which is mostly balanced by the anomalous moisture flux convergence. We have analyzed the anomalous moisture flux and its convergence in both the PBL and the free atmosphere. The magnitude of the anomalous moisture flux is generally smaller in the PBL than in the free atmosphere. We have found, however, that the anomalous

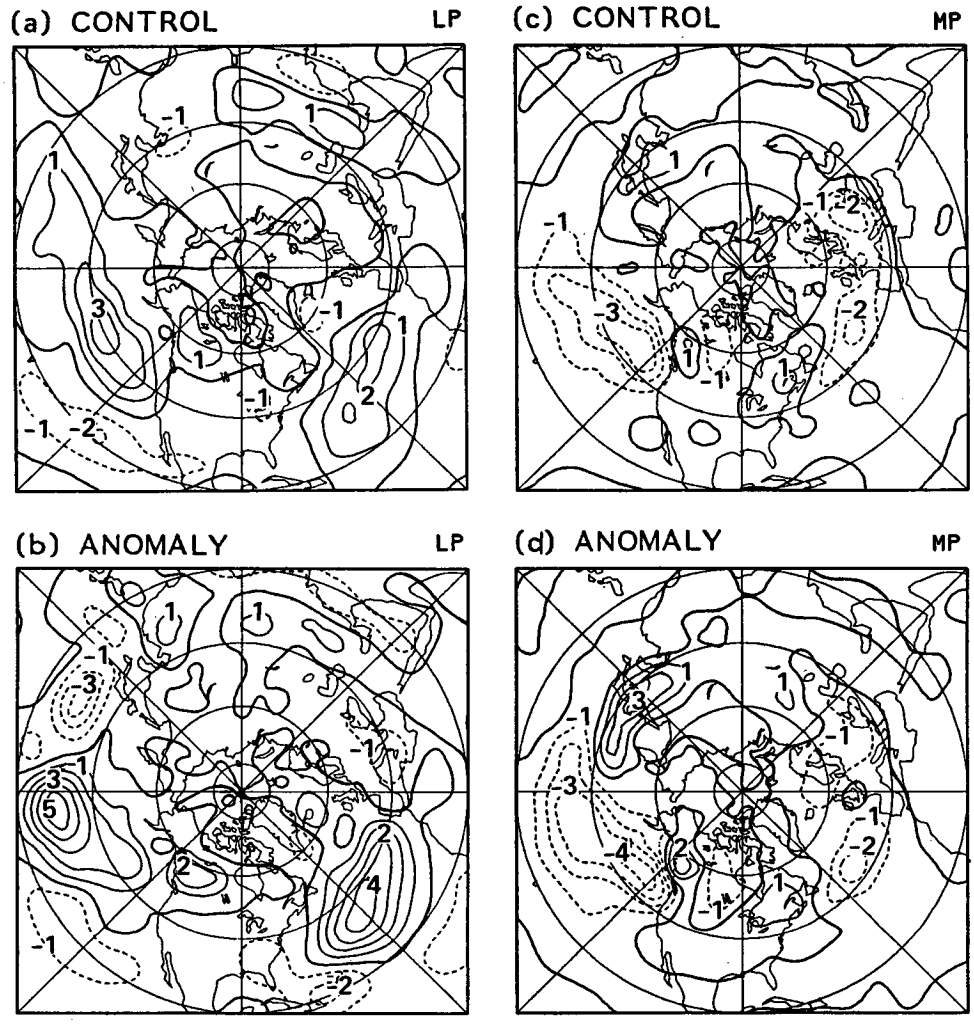

FIG. 20. As in Fig. 19, except for barotropic conversion from mean flow to eddies. Contour interval: 10^{-4} m^2 s^{-3}. Negative values are dashed.

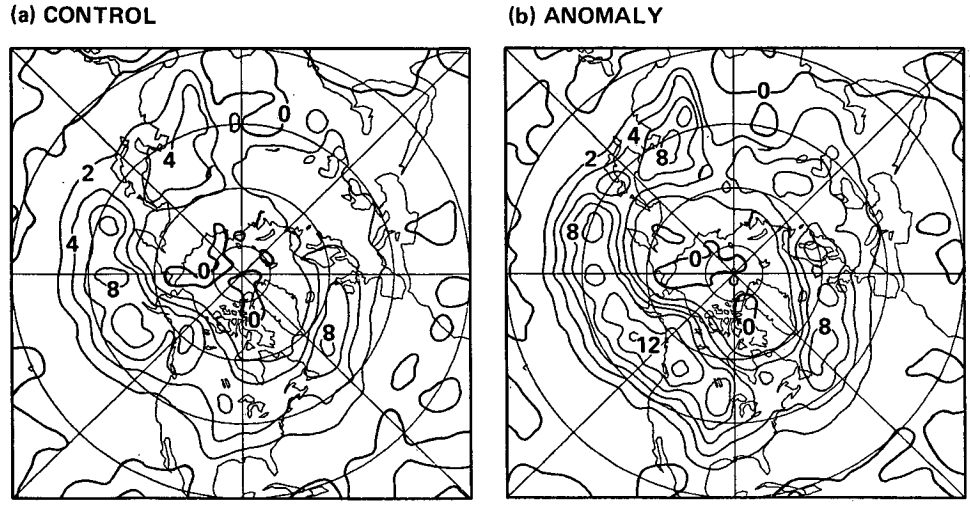

FIG. 21. Northward heat transport (m s^{-1} K) at 700 mb by medium-pass eddies for (a) control and (b) anomaly. Contour interval: 2 m s^{-1} K.

moisture flux convergence in the PBL and that in the free atmosphere have comparable magnitude with quite different geographical distribution. These findings suggest that a correct simulation of the moisture flux *both in the PBL and the free atmosphere* is crucial in determining the correct anomalous precipitation. They also suggest that anomalous tropical cumulus heating cannot be related exclusively to either flow anomalies in the PBL or in the free atmosphere.

For the midlatitudes, we have found that the response to the SSTA resembles the PNA pattern, although its features are more zonally elongated than those observed. We have also found that the midlatitude westerlies are enhanced over the Pacific, leading to an increase in the synoptic-scale transient baroclinic waves. This increase is consistent with interannual differences in the spectral distributions of transients for five winters, two of which were El Niño winters. Geographically, the increase occurs in a zonal belt extending from the northeastern Pacific to the Northern Atlantic. Over the United States in particular, this region appears to be north of that in which an increase in the activity of baroclinic waves was observed during El Niño winters.

The results presented in this paper correspond to a single pair of control-anomaly experiments. An assessment of their statistical significance requires an ensemble of such pairs. We have not performed additional experiments with the same version of the GCM. However, we have performed a pair of experiments similar to those reported here with each of the low-resolution 9- and 15-layer versions of the GCM, and many pairs with other distributions of SSTA for the mature phase of El Niño. In all cases, whose detailed analysis will be presented elsewhere, we have obtained results which are qualitatively the same for both the tropical and global response as those described in this paper, with some quantitative differences depending on the SSTA distribution and the version of the GCM. We have also found significant variability between experiments, particularly in the transient response to the SSTA. An assessment of the representativeness of this component of the response requires, therefore, additional experiments with the same version of the GCM used in this study.

Acknowledgments. We are grateful to Mr. J. A. Spahr for programming assistance. Ms. C. Wong and Ms. J. Lueken typed the manuscript. This material is based upon work supported jointly by the National Science Foundation and the National Oceanic and Atmospheric Administration under Grant ATM 8218215 and the Naval Environmental Prediction Research Facility, Monterey, California, under Program Element 62759N, Project WF59-551, "Meteorological Models and Predictions", and by the National Science Foundation under Grant ATM 8302748.

REFERENCES

Arakawa, A., and W. H. Schubert, 1974: Interaction of a cumulus cloud ensemble with the large-scale environment, Part I. *J. Atmos. Sci.*, **31**, 674–701.

——, and V. R. Lamb, 1981: A potential enstrophy and energy-conserving scheme for the shallow water equations. *Mon. Wea. Rev.*, **109**, 18–36.

——, and M. J. Suarez, 1983: Vertical differencing of the primitive equations in sigma coordinates. *Mon. Wea. Rev.*, **111**, 34–45.

Angell, J. K., 1981: Comparison of variation in atmospheric quantities with sea surface temperature variations in the equatorial eastern Pacific. *Mon. Wea. Rev.*, **109**, 230–243.

Bjerknes, J., 1969: Atmospheric teleconnections from the equatorial Pacific. *Mon. Wea. Rev.*, **97**, 163–172.

Blackmon, M. L., 1976: A climatological spectral study of the 500 mb geopotential height of the Northern Hemisphere. *J. Atmos. Sci.*, **33**, 1607–1623.

——, J. E. Geisler and E. J. Pitcher, 1983: A general circulation study of January climate anomaly patterns associated with interannual variation of equatorial Pacific sea surface temperatures. *J. Atmos. Sci.*, **40**, 1410–1425.

Cornejo-Garrido, A. G., and P. H. Stone, 1977: On the heat balance of the Walker Circulation. *J. Atmos. Sci.*, **34**, 1155–1162.

Deardorff, J. W., 1972: Parameterization of the planetary boundary layer for use in general circulation models. *Mon. Wea. Rev.*, **100**, 93–106.

Fraedrich, K., and H. Böttger, 1978: A wavenumber–frequency analysis of the 500 mb geopotential at 50°N. *J. Atmos. Sci.*, **35**, 745–750.

Geisler, J. E., M. L. Blackmon, G. T. Bates and S. Muñoz, 1985: Sensitivity of January climate response to the magnitude and position of equatorial Pacific sea surface temperature anomalies. *J. Atmos. Sci.*, **42**, 1037–1049.

Hayashi, Y., 1971: A generalized method of resolving disturbances into progressive and retrogressive waves by space-Fourier and time cross-spectral analysis. *J. Meteor. Soc. Japan*, **49**, 125–128.

Horel, J. D., and J. M. Wallace, 1981: Planetary-scale atmospheric phenomena associated with the Southern Oscillation. *Mon. Wea. Rev.*, **109**, 813–829.

Hoskins, B. J., I. N. James and G. H. White, 1983: The shape, propagation and mean-flow interaction of large-scale weather systems. *J. Atmos. Sci.*, **40**, 1595–1612.

Julian, P. R., and R. M. Chervin, 1978: A study of the Southern Oscillation and Walker circulation phenomenon. *Mon. Wea. Rev.*, **106**, 1433–1451.

Keshavamurty, R. N., 1982: Response of the atmosphere to sea surface temperature anomalies over the equatorial Pacific and the teleconnections of the Southern Oscillation. *J. Atmos. Sci.*, **39**, 1241–1259.

Mechoso, C. R., K. Yamazaki, A. Kitoh and A. Arakawa, 1985: Numerical forecasts of stratospheric warming events during the winter of 1979. *Mon. Wea. Rev.*, **113**, 1015–1029.

——, ——, —— and ——, 1986: Numerical forecasts of tropospheric and stratospheric events during the winter of 1979: Sensitivity to the model's horizontal resolution and vertical extent. *Adv. Geophys.*, **29**, 375–413.

Oort, A. H., 1983: Global atmospheric circulation statistics, 1958–1973, NOAA Professional Paper 14, U.S. Department of Commerce, Washington, DC, 180 pp.

Palmer, T. N., and D. A. Mansfield, 1986a: A study of winter time circulation anomalies during past El Niño events, using a high-resolution general circulation model. I: Influence of model climatology. *Quart. J. Roy. Meteor. Soc.*, **112**, 613–638.

——, and ——, 1986b: A study of wintertime circulation anomalies during past El Niño events, using a high-resolution general circulation model. II: Variability of the seasonal mean response. *Quart. J. Roy. Meteor. Soc.*, **112**, 639–660.

Quiroz, R. S., 1983: The climate of the "El Niño" winter of 1982–1983: A season of extraordinary anomalies. *Mon. Wea. Rev.*, **111**, 1685–1706.

Randall, D. A., 1979: The entraining moist boundary layer. *Preprints, Fourth Symp. Turbulence, Diffusion and Air Pollution,* Reno, Amer. Meteor. Soc., 467–470.

——, J. A. Abeles and T. G. Corsetti, 1985: Seasonal simulations of the planetary boundary layer and boundary layer stratocumulus clouds with a general circulation model. *J. Atmos. Sci.,* **42,** 641–676.

Rasmusson, E. M., and T. H. Carpenter, 1982: Variations in tropical sea surface temperature and surface wind fields associated with the Southern Oscillation/El Niño. *Mon. Wea. Rev.,* **110,** 354–384.

Shukla, J., and J. M. Wallace, 1983: Numerical simulation of the atmospheric response to equatorial Pacific sea surface temperature anomalies. *J. Atmos. Sci.,* **40,** 1613–1630.

Simmons, A. J., J. M. Wallace and G. W. Branstator, 1983: Barotropic wave propagation and instability, and atmospheric teleconnection patterns. *J. Atmos. Sci.,* **40,** 1363–1392.

Suarez, M. J., A. Arakawa and D. A. Randall, 1983: The parameterization of the planetary boundary layer in the UCLA general circulation model: Formulation and results. *Mon. Wea. Rev.,* **111,** 2224–2243.

Tokioka, T., K. Yamazaki and M. Chiba, 1985a: Atmospheric response to the sea surface temperature anomalies observed in early summer of 1983: A numerical experiment. *J. Meteor. Soc. Japan,* **63,** 565–588.

——, A. Kitoh and A. Katayama, 1985b: Atmospheric response to the sea surface temperature anomalies in the mature phase of El Niño under perpetual January condition. *J. Meteor. Soc. Japan,* **64,** 347–362.

Wallace, J. M., and D. S. Gutzler, 1981: Teleconnections to the geopotential height field during the Northern Hemisphere winter. *Mon. Wea. Rev.,* **109,** 784–812.